

>>>>>>>>>>>>>>>> File 1 Final version of the manuscript <<<<<<<<<<<<<<<

1

A Mechanism-image Fusion Approach to Calibration of An Ultrasound-guided Dual-arm Robotic Brachytherapy System

Jing Xiong[†], Member, IEEE, Changfu Xu[†], Khalil Ibrahim, Hao Deng,
and Zeyang Xia*, Senior Member, IEEE

Abstract—Implementation of robotic systems has significantly improved the flexibility and accuracy of prostate brachytherapy. In our previous study, an ultrasound (US)-guided dual-arm robotic brachytherapy system was developed. This system was integrated with an end-effector for needle insertion and an end-effector for US probe. The calibration accuracy of the system determines the effectiveness of the whole system. However, existing calibration methods are mechanism-based calibration methods or image-based calibration methods. With these methods, external tracker and complex phantom are needed, which may result in accumulative errors. Therefore, this paper presents a mechanism-image fusion approach to calibration of a US-guided dual-arm robotic brachytherapy system. With this approach, no tracker or complex phantom is needed as the dual-arm robotic system can use one arm as a substitute for tracker and phantom to calibrate the other arm. The needle-tip positions localized by the mechanism and image are utilized while the needle is also the controlled object of needle insertion. Experiments using three registration algorithms were performed, and results were evaluated utilizing the leave-one-out cross-validation method. The results showed that the calibration accuracy of the whole system is 0.65 ± 0.31 mm. Additional experimental and parametrical comparisons of the proposed method with the state-of-the-art methods were conducted, and the results justified the outperformance of the proposed method.

Index Terms—Calibration approach, dual-arm robotic system, mechanism-image fusion, ultrasound-guided brachytherapy.

This work was supported in part by the National Key R&D Program of China (2017YFC0110402), in part by the National Natural Science Foundation of China (62073309, 61773365, U2013205), in part by the Fundamental Research Program of Shenzhen (JCYJ20170413162458312), and in part by the Chinese Academy of Sciences Youth Innovation Promotion Association Excellent Member Program (Y201968). ([†] These authors contributed equally to this work. * Corresponding author: Zeyang Xia.).

J. Xiong, C. Xu, and K. Ibrahim are with Shenzhen Institutes of Advanced Technology, Chinese Academy of Sciences, Shenzhen 518055, China (e-mails: {jing.xiong, cf.xu, ibrahim}@siat.ac.cn).

H. Deng is with Shenzhen Institutes of Advanced Technology, Chinese Academy of Sciences, and University of Chinese Academy of Sciences, Shenzhen 518055, China (e-mail: hao.deng@siat.ac.cn).

Z. Xia is with Shenzhen Institutes of Advanced Technology, Chinese Academy of Sciences, and the CAS Key Laboratory of Human-Machine Intelligence-Synergy Systems, Shenzhen Institutes of Advanced Technology, Shenzhen 518055, China (e-mail: zy.xia@siat.ac.cn).

I. INTRODUCTION

PROSTATE cancer is a prevalent cancer among men. According to surveys [1, 2], prostate cancer may be diagnosed in 1 out of 9 men during their lifetimes. The American Cancer Society's estimates for prostate cancer in the United States for the year 2020 are about 191,930 new cases and about 33,330 deaths. Brachytherapy was proposed to treat prostate cancer and has already benefitted a significant portion of the population for treating cancer and maintaining their quality lives [3-5]. The permanent low-dose-rate brachytherapy is the primary treatment for prostate cancer that benefits intense localized therapy in the prostate and has a shorter hospitalization period (1 to 2 days) than external beam radiation therapy. But this method usually needs the permanent insertion of around 100 tiny radioactive seeds for the localized irradiation of the prostate, which results in many side effects, instabilities and high-cost procedures [6, 7]. In recent years, robotic systems have been introduced to improve prostate brachytherapy accuracy [8-12]. In particular, the dual-arm robotic system has a significant advantage in the image-guided brachytherapy field because the integrated ultrasound (US) probe and the needle are controlled separately to realize various needle insertion angles in a very narrow space [13, 14]. Therefore, a US-guided dual-arm robotic brachytherapy system was developed in our previous study, where the calibration accuracy of the system directly influences the effectiveness of the whole system.

Existing calibration methods can be roughly classified into two categories, mechanism-based calibration and image-based calibration. (I) The mechanism-based calibration method is mainly used for robotic system calibration [15, 16]. In mechanism-based calibration, Wang *et al.* [15] proposed a calibration method for the multiple cooperative robots. In this method, the calibration problem for multiple robot cooperation was formulated as a fundamental problem of solving a matrix equation $AXB = YCZ$, and an efficient iterative solution was used. But this method usually requires good initial estimates that are not always easy or possible to be obtained. To address this, Ma *et al.* [16] proposed a probabilistic approach of solving the $AXB = YCZ$ calibration problem without a priori knowledge of the temporal correspondence of the data.

However, with these exiting methods, an external tracker, such as camera is needed, which results in accumulative errors. (II) The image-based calibration method is mainly used for US probe calibration [17-30]. In image-based calibration, most calibration methods require a phantom to provide a set of fiducials, where the N-wire phantom method is a traditional US calibration method [20, 21]. To avoid the isotropic fiducial localization errors, Carbajal *et al.* [22] proposed an improved N-wire phantom freehand US calibration method based on the middle wires and improved the calibration accuracy. Afterward, Najafi *et al.* [25] proposed a multi-wedge phantom calibration method to achieve higher calibration accuracy. In this method, the calibration matrix was solved with a closed-form solution, which enables easy, fast, and accurate US calibration. Recently, inspired by Carbajal *et al.* [22], Shen *et al.* [27] proposed a novel method that considered all the wires to perform probe calibration and achieved better results. However, with these existing methods, external tracker and wire/wedge phantom are needed, which also may result in accumulative errors. Besides, Hungr *et al.* [31] constructed a small rubber sleeve with a softball at the needle end, which improved the localization of the needle-tip of US images in the water, but also resulted in extra errors due to the softball simultaneously. Kim *et al.* [32] used a planar surface mockup as a phantom, which also brought in extra errors due to the mockup. Afterward, this calibration method [32] was applied to a robot-assisted approach for transrectal ultrasound (TRUS) guided prostate biopsy [33], and the results showed that this approach is feasible and has the potential to significantly increase the detection of prostate cancer.

In summary, these existing methods were mechanism-based calibration methods or image-based calibration methods, which needed external tracker and complex phantom, as shown in Fig. 1. With these methods, external tracker and complex phantom may result in accumulative errors. As a result, they cannot ensure a sufficiently high calibration accuracy. Therefore, we present a mechanism-image fusion-based calibration approach to a US-guided dual-arm robotic brachytherapy system in this paper. In this approach, one arm of the dual-arm robotic system is used as a substitute for tracker and phantom to calibrate the other arm, which will ensure a sufficiently high calibration accuracy for the US-guided dual-arm robotic brachytherapy system. The effectiveness of the proposed calibration approach was validated through experiments in our developed US-guided dual-arm robotic brachytherapy system using three registration algorithms. Additional experimental and parametrical comparisons of the proposed method with state-of-the-art methods were conducted to thoroughly evaluate the outperformance of the proposed method.

The rest of this paper is organized as follows: Section II describes the proposed mechanism-image fusion approach to calibration of a US-guided dual-arm robotic brachytherapy system. The experiments and results are presented in Section III. The discussion about the proposed approach's characteristics is presented in Section IV before the conclusion and future work of this paper in Section V.

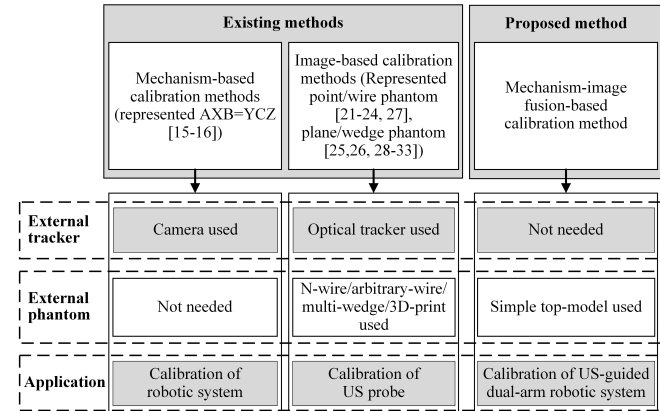


Fig. 1. Comparison of the proposed method with existing methods.

II. MECHANISM-IMAGE FUSION CALIBRATION APPROACH

A. US-guided Dual-arm Robotic Brachytherapy System

Previously we developed a US-guided dual-arm robotic system (see Fig. 2), which consists of a dual-arm robotic system, a US machine with a 2D US probe, and two end-effectors. The schematic of this system is shown in Fig. 3. Some details about the specific parts of the robotic setup are given below.

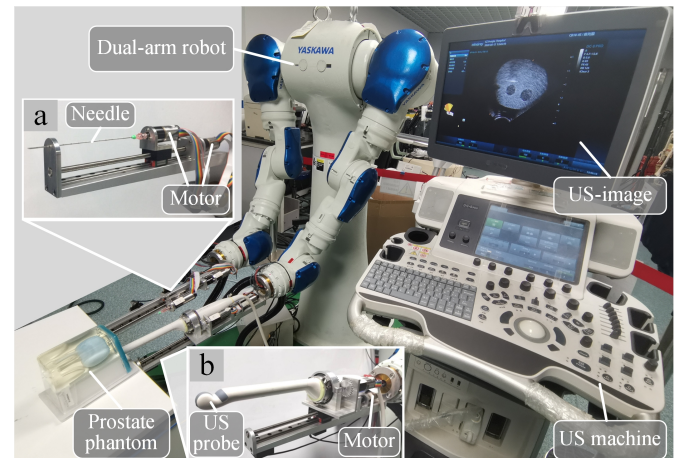


Fig. 2. A US-guided dual-arm robotic system for prostate brachytherapy. (a) The needle end-effector. (b) The ultrasound probe end-effector.

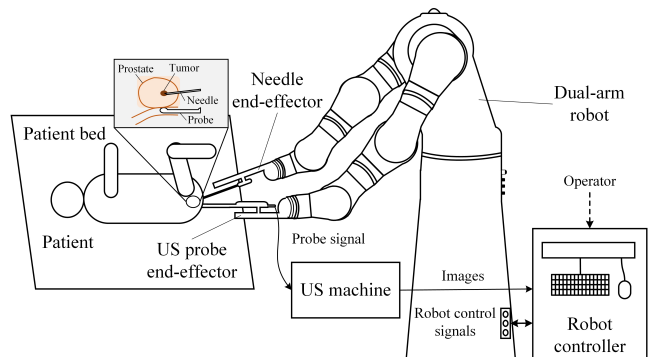


Fig. 3. Schematic of the US-guided dual-arm robotic system for prostate brachytherapy.

1) Dual-arm robotic system: The dual-arm robotic system consists of a robot controller with a robot operating system

>>>>>>>>>>>>>> File 1 Final version of the manuscript <<<<<<<<<<<<<<

3

(ROS) and a dual-arm robot (YASKAWA SDA10F [34]), which was integrated with an end-effector for needle insertion (defined as needle end-effector) and an end-effector for US probe (defined as US probe end-effector) on each arm, respectively. The needle end-effector consists of an inserting needle and two motors (see Fig. 2(a)) and is mounted onto the end-flange of the right robotic arm for needle insertion. The two motors drive the needle to move forward and to rotate, respectively. Here, to reduce the prostate deformation in the insertion process, the rotation motor is only used to drive the needle's rotation while being inserted into the prostate. The US probe end-effector mainly consists of a US-probe and a motor (see Fig. 2(b)) and is mounted onto the left robotic arm's end flange for TRUS scanning. The motor is used to drive the needle to move forward.

2) US machine: A DC-80 PRO color Doppler US machine with a CB10-4E 2D US probe (Mindray Medical Corporation, Shenzhen, China) was integrated into the robotic setup to acquire US image sequences. The US probe's central frequency is 6.5 MHz and its field of view is $2\pi/3$ radians. The US image has a 1080×720 resolution with 0.19 mm/pixel and a 7 cm reflex depth.

In the US-guided dual-arm robotic brachytherapy system, the needle end-effector and US probe end-effector are controlled separately. The needle-tip needs to be accurately inserted into the prostate tumor. Therefore, the whole system needs to be ensured in high calibration accuracy. The following section will describe the proposed mechanism-image fusion-based calibration approach to a US-guided dual-arm robotic brachytherapy system.

B. The Overall Framework of Calibration Approach

Unlike single-arm robotic systems, we observed that the dual-arm robotic system can use one arm as a substitute for tracker and phantom to calibrate the other arm. Therefore, the arm integrated needle end-effector of the dual-arm robotic system is used as a substitute for tracker and phantom to calibrate the other arm integrated US probe end-effector. The transformations involved in the US-guided dual-arm robotic brachytherapy system are shown in Fig. 4. The dual-arm robotic system includes two robotic arms with the same base frame (defined as R frame). Therefore, the needle-tip position in R frame can be calculated by two transformation routes relative to the needle end-effector and the US probe end-effector, respectively, as shown in equation (1).

$${}^R\mathbf{T}_{ER} \cdot {}^{ER}\mathbf{P}_{Ntip} = {}^R\mathbf{T}_{EL} \cdot {}^{EL}\mathbf{T}_{Ptip} \cdot {}^{Ptip}\mathbf{T}_I \cdot {}^I\mathbf{P}_{Ntip} \quad (1)$$

where ${}^{ER}\mathbf{P}_{Ntip}$ is the position vector of the needle-tip (defined as $Ntip$ frame) relative to the end-flange frame of the right robotic arm (defined as ER frame); ${}^R\mathbf{T}_{ER}$ is the transformation matrix of ER frame relative to R frame; ${}^I\mathbf{P}_{Ntip}$ is the position vector of needle-tip in I frame (defined as I frame); ${}^{Ptip}\mathbf{T}_I$ is the transformation matrix of I frame relative to the US probe-tip frame (defined as $Ptip$ frame); ${}^{EL}\mathbf{T}_{Ptip}$ is the transformation matrix of $Ptip$ frame relative to the end-flange frame of the left robotic arm (defined as EL frame), ${}^R\mathbf{T}_{EL}$ is the transformation matrix of EL frame relative to R frame. Furthermore, ${}^R\mathbf{T}_{ER}$ and

${}^R\mathbf{T}_{EL}$ are obtained by ROS directly; ${}^I\mathbf{P}_{Ntip}$ is calculated by manual annotation in the US image of needle-tip. The ${}^{ER}\mathbf{P}_{Ntip}$, ${}^{EL}\mathbf{T}_{Ptip}$, and ${}^{Ptip}\mathbf{T}_I$ are unknown and should be calibrated in this system. Here, the probe-tip (see Fig. 6(c) and Fig. 8(c)) is designed and fixed on the US probe instead of using the external tracker and will be removed after calibration.

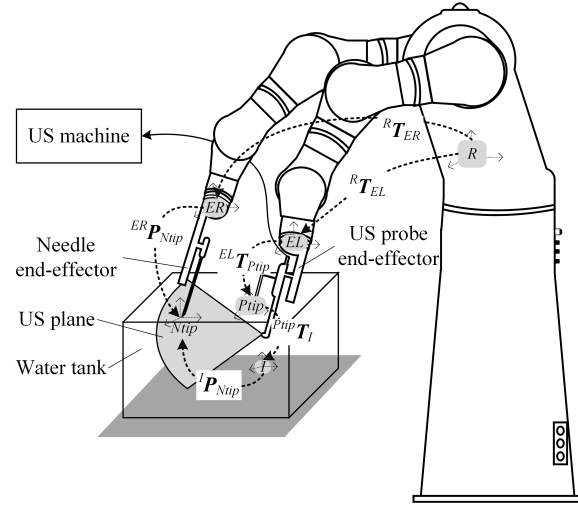


Fig. 4. Transformations involved in the US-guided dual-arm robotic brachytherapy system. (R : Robotic base frame. ER : End-flange frame of the right robotic arm. EL : End-flange frame of the left robotic arm. $Ntip$: Needle-tip frame. $Ptip$: Ultrasound probe-tip frame. I : Ultrasound image frame.)

Mechanical calibration

Build the position calibration model, and calibrate the position vectors, ${}^{ER}\mathbf{P}_{Ntip}$ and ${}^{EL}\mathbf{P}_{Ptip}$, of the $Ntip$ frame to ER frame and the $Ptip$ frame to EL frame, respectively.

Build the posture calibration model, and calibrate the rotational matrices, ${}^{ER}\mathbf{R}_{Ntip}$ and ${}^{EL}\mathbf{R}_{Ptip}$, of the $Ntip$ frame to ER frame and the $Ptip$ frame to EL frame, respectively.

US probe calibration

Control the US probe to scan the needle and take the sample data, including the position vector ${}^I\mathbf{P}_{Ntip}$ of the $Ntip$ frame to I frame, the transformation matrix ${}^R\mathbf{T}_{EL}$ of the EL frame to R frame, and the transformation matrix ${}^R\mathbf{T}_{ER}$ of the ER frame to R frame.

Build mechanism-image fusion model of calibration based on the mechanical calibration results, sample data, and equation (1).

Solve the rigid transformation matrix ${}^{Ptip}\mathbf{T}_I$ of I frame relative to $Ptip$ frame by using the registration algorithm.

Fig. 5. The overall framework of the proposed calibration approach. (R : Robotic base frame. ER : End-flange frame of the right robotic arm. EL : End-flange frame of the left robotic arm. $Ntip$: Needle-tip frame. $Ptip$: Ultrasound probe-tip frame. I : Ultrasound image frame.)

Based on the above analysis, a mechanism-image fusion approach to calibration of the ${}^{ER}\mathbf{T}_{Ntip}$, ${}^{EL}\mathbf{T}_{Ptip}$, and ${}^{Ptip}\mathbf{T}_I$ is designed in this paper. The overall framework of the proposed calibration approach is shown in Fig. 5. Firstly, the ${}^{ER}\mathbf{P}_{Ntip}$ and ${}^{EL}\mathbf{P}_{Ptip}$ are calibrated by building the position and posture calibration model, respectively, in the mechanical calibration

process. Secondly, based on the mechanical calibration results, sample data, and equation (1), the US probe calibration is built as a registration model [36]. Finally, the transformation matrix ${}^{P_{tip}}T_I$ of the US probe calibration can be solved using a registration algorithm. Here, the US probe is calibrated based on the needle localization while the needle is also the controlled object of needle insertion. Therefore, the calibration accuracy of this approach could also benefit the needle insertion application. The specific modeling and implementation of the mechanical calibration and US probe calibration are described in the next two sections.

C. Mechanical Calibration Modeling and Implementation

The rigid transformation matrices of ${}^{ER}T_{Ntip}$ and ${}^{EL}T_{Ptip}$ are calibrated by building the position and posture calibration model in this part. According to robot kinematics, the ${}^{ER}T_{Ntip}$ and ${}^{EL}T_{Ptip}$ can be represented in (2) and (3), respectively.

$${}^{ER}T_{Ntip} = \begin{bmatrix} {}^{ER}R_{Ntip} & {}^{ER}P_{Ntip} \\ 0_{1 \times 3} & 1 \end{bmatrix} \quad (2)$$

$${}^{EL}T_{Ptip} = \begin{bmatrix} {}^{EL}R_{Ptip} & {}^{EL}P_{Ptip} \\ 0_{1 \times 3} & 1 \end{bmatrix} \quad (3)$$

where ${}^{ER}R_{Ntip}$ and ${}^{EL}R_{Ptip}$ are the rotational matrices of the N_{tip} frame relative to ER frame and P_{tip} frame relative to EL frame, respectively; ${}^{ER}P_{Ntip}$ and ${}^{EL}P_{Ptip}$ are the position vectors of the N_{tip} frame relative to ER frame and P_{tip} frame relative to EL frame, respectively.

1) Position vector calibration: We observed that the robotic arm can be a localizer due to the robotic system's high accuracy. Thus, a top-model (see Fig. 6(a) and Fig. 8(a)) is adopted to calibrate the position vectors of ${}^{ER}P_{Ntip}$ and ${}^{EL}P_{Ptip}$. This top-model is designed with CAD and fixed on the end-flange of the dual-arm robot. The processed sketch of mechanical calibration is shown in Fig. 6. Here, the top-model is designed and finished with high accuracy by the factory. Hence, the top-model parameter is calculated by combining the CAD size and testing error size. That is to say, when the top-model is fixed on the robotic end-flange, the model-tip's (defined as M_{tip} frame) position ${}^{ER}P_{Mtip}$ in the ER frame is known. Therefore, when the model-tip is controlled to reach the reference-tip position, the reference-tip position ${}^R P_{Rtip}$ in R frame is represented in (4). After, the top-model is removed, and the needle end-effector and US probe end-effector are fixed on the right and left robotic arm, respectively. Similarly, when the needle-tip and US probe-tip are controlled to reach the reference-tip position, the needle-tip position ${}^R P_{Ntip}$ and US probe-tip position ${}^R P_{Ptip}$ in R frame can be obtained and are represented in (5) and (6), respectively.

$${}^R P_{Rtip} = {}^R T_{ER} \cdot {}^{ER} P_{Mtip} \quad (4)$$

$${}^R P_{Ntip} = {}^R T_{ER} \cdot {}^{ER} P_{Ntip} = {}^R P_{Rtip} \quad (5)$$

$${}^R P_{Ptip} = {}^R T_{EL} \cdot {}^{EL} P_{Ptip} = {}^R P_{Rtip} \quad (6)$$

Then based on (4), (5), (6), and matrix operations, the ${}^{ER}P_{Ntip}$ is calculated by $\text{inv}({}^R T_{ER}) \cdot {}^R P_{Rtip}$. The ${}^{EL}P_{Ptip}$ is calculated by $\text{inv}({}^R T_{EL}) \cdot {}^R P_{Rtip}$. The $\text{inv}()$ stands for computing the inverse of

the matrix.

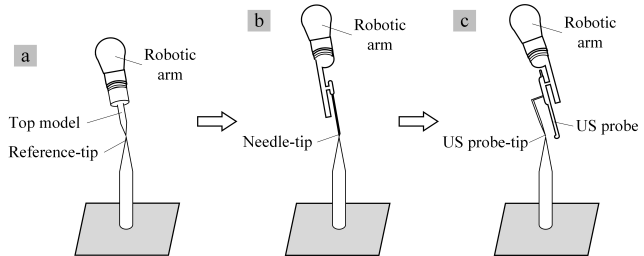


Fig. 6. The procedure of mechanical calibration. (a) Moving the top-model-tip to reference-tip. (b) Moving the needle-tip to reference-tip. (c) Moving the ultrasound probe-tip to reference-tip.

2) Rotational matrix calibration: Generally, the end-effector frame is the same as the end-flange frame at default. However, to get high calibration accuracy, the robotic tool control frame calibration method [35] is adopted to calibrate the rotational matrices of ${}^{ER}R_{Ntip}$ and ${}^{EL}R_{Ptip}$ as follows:

Step1: The needle-tip is controlled to be positioned at a point p_1 by the dual-arm robotic system, and then the rotational matrix ${}^R R_{ER1}$ and position vector ${}^R P_{ER1}$ of ER frame relative to R frame can be obtained from the ROS. The p_1 position in R frame is calculated by ${}^R P_1 = {}^R R_{ER1} \cdot {}^{ER} P_{Ntip} + {}^R P_{ER1}$ according to the results of needle-tip calibration.

Step2: The needle-tip is controlled to be positioned at another point p_2 by the dual-arm robotic system, and this translational direction from p_1 to p_2 is defined as the y axial of the N_{tip} frame. Similarly, the p_2 position in R frame is calculated by ${}^R P_2 = {}^R R_{ER2} \cdot {}^{ER} P_{Ntip} + {}^R P_{ER2}$ according to the results of needle-tip calibration, where ${}^R R_{ER2}$ and ${}^R P_{ER2}$ are the rotational matrix and position vector, respectively, of ER frame relative to R frame.

Step3: According to coordinate transformation relation of robot kinematics, the y -directional unit vector N_y of the N_{tip} frame relative to R frame can be calculated in two different ways, $N_y = ({}^R P_2 - {}^R P_1) / \| {}^R P_2 - {}^R P_1 \|$ and $N_y = {}^R R_{ER1} \cdot n_y$, where n_y is the y -directional unit vector of the N_{tip} frame relative to ER frame. Therefore, based on the above two equations, n_y is calculated by

$$n_y = \text{inv}({}^R R_{ER1}) \cdot N_y \quad (7)$$

Step4: The needle-tip is controlled to be positioned at another point p_3 by the dual-arm robotic system, and this translational direction from p_1 to p_3 is defined as the z axial of the N_{tip} frame. Similar to the above steps of calculating n_y , the z -direction unit vector n_z of the N_{tip} frame relative to ER frame can be calculated.

Step5: Based on the above equations, the x -directional unit vector n_x of N_{tip} frame is calculated by $n_x = n_y \times n_z$, and the z -directional unit vector n_z should be updated by $n_z = n_x \times n_y$ to keep the mutual orthogonality of n_x , n_y and n_z . Then according to the robot kinematics, the rotational matrix of the N_{tip} frame relative to ER frame can be represented by ${}^{ER}R_{Ntip} = [n_x, n_y, n_z]_{3 \times 3}$. Similarly, we can calibrate the ${}^{EL}R_{Ptip}$. Finally, based on the calibration results of position vectors (${}^{ER}P_{Ntip}$ and ${}^{EL}P_{Ptip}$) and rotational matrices (${}^{ER}R_{Ntip}$ and ${}^{EL}R_{Ptip}$), the transformation

matrices ${}^R\mathbf{T}_{Ntip}$ and ${}^{EL}\mathbf{T}_{Ptip}$ can be calculated by equation (2) and (3), respectively.

D. US Probe Calibration Modeling and Implementation

To calibrate the US probe, the arm integrated with the needle end-effector of the dual-arm robotic system is used as a substitute for tracker and phantom. The US probe calibration framework is built, as shown in Fig. 7. The calibration process mainly includes three steps: data acquisition, data processing, and calibration modeling and implementation.

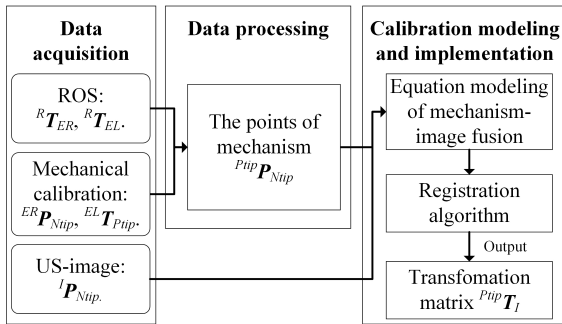


Fig. 7. The framework of US probe calibration. (R : Robotic base frame. ER : End-flange frame of the right robotic arm. EL : End-flange frame of the left robotic arm. $Ntip$: Needle-tip frame. $Ptip$: Ultrasound probe-tip frame. I : Ultrasound image frame.)

1) Data acquisition: The sample data is taken in this step, including the needle-tip's position vector ${}^R\mathbf{P}_{Ntip}$ in R frame, the transformation matrix ${}^R\mathbf{T}_{ER}$ of the ER frame relative to R frame, the needle-tip's position vector ${}^I\mathbf{P}_{Ntip}$ in the I frame, the transformation matrix ${}^{EL}\mathbf{T}_{Ptip}$ of the $Ptip$ frame relative to EL frame, the transformation matrix ${}^R\mathbf{T}_{EL}$ of the EL frame relative to R frame. Here, the ${}^R\mathbf{T}_{ER}$ and ${}^R\mathbf{T}_{EL}$ are achieved by ROS directly. The ${}^R\mathbf{P}_{Ntip}$ and ${}^{EL}\mathbf{P}_{Ptip}$ have been solved in the previous section. The ${}^I\mathbf{P}_{Ntip}$ is calculated by manual annotation in the US image of the needle-tip.

2) Data Processing: The point set ${}^{Ptip}\mathbf{P}_{Ntip}$ is calculated in this step. Firstly, equation (8) is achieved because the needle-tip position in R frame can be calculated by two transformation routes relative to the needle end-effector and the US probe end-effector, respectively.

$${}^R\mathbf{T}_{ER} \cdot {}^R\mathbf{P}_{Ntip} = {}^R\mathbf{T}_{EL} \cdot {}^{EL}\mathbf{T}_{Ptip} \cdot {}^{Ptip}\mathbf{P}_{Ntip} \quad (8)$$

Then based on (8), the ${}^{Ptip}\mathbf{P}_{Ntip}$ is calculated by $inv({}^R\mathbf{T}_{EL} \cdot {}^{EL}\mathbf{T}_{Ptip}) \cdot {}^R\mathbf{T}_{ER} \cdot {}^R\mathbf{P}_{Ntip}$.

3) Calibration modeling and implementation: Inspired by the problem of point cloud registration [36], the US probe is calibrated by building a registration model based on the ${}^{Ptip}\mathbf{P}_{Ntip}$ and ${}^I\mathbf{P}_{Ntip}$. This model is represented by

$${}^{Ptip}\mathbf{P}_{Ntip} = {}^{Ptip}\mathbf{T}_I \cdot {}^I\mathbf{P}_{Ntip}. \quad (9)$$

Then ${}^{Ptip}\mathbf{T}_I$ can be solved by the point-to-point registration algorithm. For example, the iterative closest point (ICP) algorithm [36]. Finally, based on the above operations, the prostate tumor's position in R frame is calculated by ${}^R\mathbf{P}_{Tumor} = {}^R\mathbf{T}_{EL} \cdot {}^{EL}\mathbf{T}_{Ptip} \cdot {}^{Ptip}\mathbf{T}_I \cdot {}^I\mathbf{P}_{Tumor}$, where ${}^I\mathbf{P}_{Tumor}$ is the prostate tumor's position in I frame and can be calculated by manual marking or image process technique.

III. EXPERIMENTS AND RESULTS

The experimental design is first introduced in this section. Then lots of experiments are conducted to evaluate the effectiveness of the proposed calibration approach, including evaluation of the mechanical calibration, evaluation of the US probe calibration, comparison of the proposed method with existing methods, and evaluation of execution time.

A. Experimental Design

The experimental setup of the overall calibration is shown in Fig. 8. In the mechanical calibration experiment, $Rtip_1$ and $Rtip_2$ are the two auxiliary reference-tips for calibration and validation, respectively (see Fig. 8(a)). As shown in Fig. 8(b) and Fig. 8(c), we first calibrated and validated the position vectors ${}^R\mathbf{P}_{Ntip}$ and ${}^{EL}\mathbf{P}_{Ptip}$ of the needle-tip relative to ER frame and US probe-tip relative to EL frame, respectively, according to the section II. C. 1). Then the rotational matrices ${}^R\mathbf{R}_{Ntip}$ and ${}^{EL}\mathbf{R}_{Ptip}$ of the needle-tip relative to ER frame and US probe-tip relative to EL frame are calibrated, respectively, according to the section II. C. 2). In the US probe calibration experiment, the environment mainly consists of a dual-arm robot, a water tank, the needle end-effector, the US probe end-effector, and a US machine (see Fig. 8(d)). Based on the mechanical calibration results, the transformation matrix ${}^{Ptip}\mathbf{T}_I$ of the I frame relative to $Ptip$ frame is calibrated according to the section II. D. The overall calibration procedure is shown in Fig. 9.

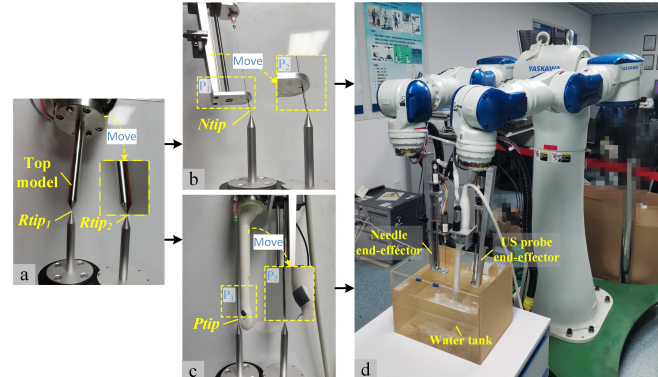


Fig. 8. The experimental setup of overall calibration. (a) Setups of moving the top-model-tip $Mtip$ to reference-tips $Rtip_1$ and $Rtip_2$. (b) Setups of moving the needle-tip $Ntip$ to reference-tips $Rtip_1$ and $Rtip_2$. (c) Setups of moving the US probe-tip $Ntip$ to reference-tips $Rtip_1$ and $Rtip_2$. (d) Setup of taking needle-tip's US image.

To ensure the evaluative reliability and reduce to the random factors' effect, the leave-one-out cross-validation [37] (LOO-CV) method is adopted. Specifically, if it has N sample points, the LOO-CV is equal to N -fold cross-validation (N-CV). That is to say, the $N-1$ samples are used as the train set, and the left one sample is used as the test set, and the N repeat experiments are taken. At the same time, the *Mean Absolute Error* (MAE) and *Root Square Mean Error* (RMSE), similarly equal to *Point Reconstruction Accuracy* (PRA) [38], and *Standard Deviation* (SD) are introduced for assessing the calibration accuracy of the proposed method. The MAE, RMSE, and SD are defined in (10), (11), and (12), respectively.

>>>>>>>>>>>>>>> File 1 Final version of the manuscript <<<<<<<<<<<<<<

6

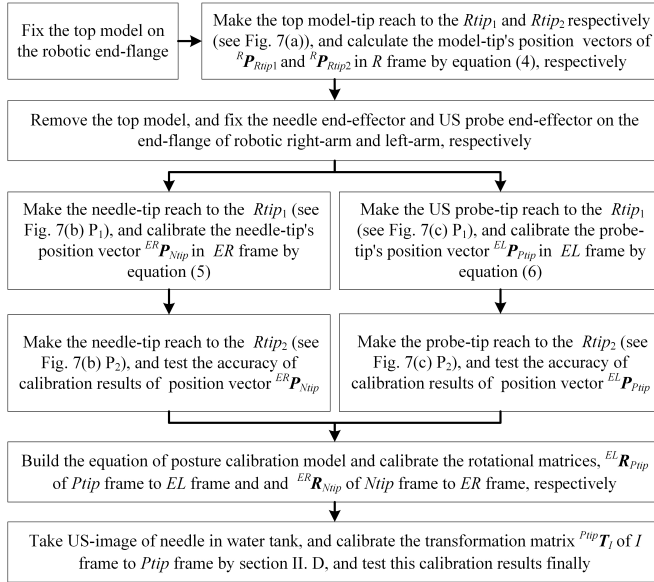


Fig. 9. The overall calibration procedure. (*R*: Robotic base frame. *ER*: End-flange frame of the right robotic arm. *EL*: End-flange frame of the left robotic arm. *Ntip*: Needle-tip frame. *Ptip*: Ultrasound probe-tip frame. *I*: Ultrasound image frame.)

$$MAE = \frac{1}{n} \sum_{i=1}^n \| \mathbf{P}_{real}(i) - \mathbf{P}_{cal}(i) \| \quad (10)$$

$$RMSE = \sqrt{\frac{1}{n} \sum_{i=1}^n \| \mathbf{P}_{real}(i) - \mathbf{P}_{cal}(i) \|^2} \quad (11)$$

$$SD = \sqrt{\frac{1}{n} \sum_{i=1}^n \| \mathbf{P}_{real}(i) - \bar{\mathbf{P}}_{cal} \|^2} \quad (12)$$

where n is the number of repeat experiments that is equal to N of N -fold cross-validation. The $\mathbf{P}_{cal}(i)$ and $\mathbf{P}_{real}(i)$ are the calculative position vector and real position vector in i th experiment, respectively. The $\bar{\mathbf{P}}_{cal}$ is the average value of the calculative position vectors of n experiments. In the process of mechanical calibration, the $\mathbf{P}_{cal}(i)$ is calculated by $\mathbf{P}_{cal}(i) = {}^R\mathbf{T}_{ER}(i) \cdot {}^{ER}\mathbf{P}_{Ntip}$. The $\mathbf{P}_{real}(i)$ is the real reference-tip $Rtip$'s position vector relative to R frame in i th experiment that can be represented by $\mathbf{P}_{real}(i) = {}^R\mathbf{T}_{ER}(i) \cdot {}^{ER}\mathbf{P}_{Mtip}$. In the process of US probe calibration, the $\mathbf{P}_{cal}(i)$ is calculated by $\mathbf{P}_{cal}(i) = {}^R\mathbf{T}_{EL}(i) \cdot {}^{EL}\mathbf{T}_{Ptip} \cdot {}^{Ptip}\mathbf{T}_I \cdot {}^I\mathbf{P}_{Ntip}(i)$. The $\mathbf{P}_{real}(i)$ is real needle-tip's position vector relative to R frame in i th experiment that can be represented by $\mathbf{P}_{real}(i) = {}^R\mathbf{T}_{ER}(i) \cdot {}^{ER}\mathbf{P}_{Ntip}$.

B. Evaluation of Mechanical Calibration

To ensure that the experimental results are reliable, we first evaluate the mechanical calibration accuracy, including needle-tip calibration and probe-tip calibration. As shown in Fig. 8(a)-(c), according to the usual condition of calibration of the traditional robot reference frame [39], it took three repeatable calibration experiments of moving the needle-tip *Ntip* and probe-tip *Ptip* to reference-tip *Rtip*, respectively, according to the mechanical calibration method. Then the average values ${}^{ER}\mathbf{P}_{Ntip}$ and ${}^{EL}\mathbf{P}_{Ntip}$ of these three calibration results are used as the needle-tip's calibration results and probe-tip's calibration results, respectively. After, we took three repeatable testing experiments of moving the needle-tip to reference-tip *Rtip* and probe-tip to reference-tip *Rtip* to

calculate the calibration accuracy of needle-tip and US probe-tip, respectively, based on the equation (10), (11), and (12). The results of calibration accuracy are shown in Table I.

TABLE I.
THE ACCURACY OF MECHANICAL CALIBRATION.

Calibration category	MAE (mm)	RMSE (mm)	SD (mm)
Needle-tip calibration	0.19	0.20	0.06
US probe-tip calibration	0.19	0.21	0.12

As shown in Table I, the *MAE*, *RMSE*, and *SD* of the needle-tip calibration are only 0.19 mm, 0.20 mm, and 0.06 mm, respectively. The *MAE*, *RMSE*, and *SD* of the probe-tip calibration are only 0.19 mm, 0.21 mm, and 0.12 mm, respectively. These results show that the calibration accuracies of needle-tip position and probe-tip position are effective and make a good foundation for the US probe calibration of the system.

C. Evaluation of US Probe Calibration

In the experiments of the US probe calibration, since the prostate volume is usually about $40*40*40$ mm³, we took 64 sample points of the needle-tip's position in *R* frame. These 64 sample points are nearly evenly distributed in the $40*40*40$ mm³ space to ensure the coverage of the prostate volume (see Fig. 10(a)). Then the three registration algorithms of ICP [36], Kabsch [40], and Landmark [41] are adopted to solve the transformation matrix $Ptip_T_I$. The LOO-CV method is adopted to take 64 repeating experiments of leave-one-out cross-validation. The experimental accuracy of US probe calibration in the whole system is shown in Table II. The distribution of sample points and calibration points in 3D space (an example of ICP algorithm) is shown in Fig. 10.

TABLE II.
THE ACCURACY OF US PROBE CALIBRATION.

Registration algorithms	Calibration accuracy of the whole system		
	MAE (mm)	RMSE (mm)	SD (mm)
ICP	0.65	0.72	0.31
Kabsch	0.65	0.71	0.30
Landmark	0.65	0.71	0.30

As shown in Table II, when the ICP algorithm is used to solve the transformation matrix of *I* frame to *Ptip* frame, the *MAE*, *RMSE*, and *SD* of US probe calibration in the whole system are 0.65 mm, 0.72 mm, and 0.31 mm, respectively. The *MAE* of US probe calibration in the whole system is the same for the three registration algorithms. The *RMSE* and *SD* of these registration algorithms are very close. At the same time, in the 64 experiments with the ICP algorithm, most of these calibration results' errors (*MAE*) are around 0.6 mm, and over half of them are less than 0.6 mm, and only two experimental errors (1.67 mm and 1.64 mm) of them are greater than 1.1 mm (see Fig. 11). Furthermore, the accuracy evaluation between truth points and calculation points are shown in Fig. 10(e). It shows that the positions of calculation points and the truth points' positions in 3D space are well registered. These results indicate that the proposed method is effective.

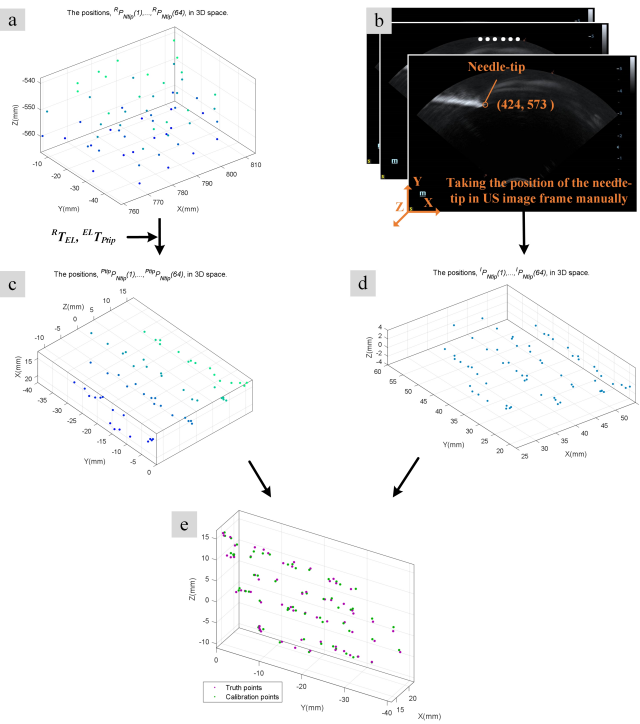


Fig. 10. The distributions of sample positions, $\{^R\mathbf{P}_{Nip}(1), \dots, ^R\mathbf{P}_{Nip}(64)\}$ (a), $\{^{Pip}\mathbf{P}_{Nip}(1), \dots, ^{Pip}\mathbf{P}_{Nip}(64)\}$ (c), and $\{^I\mathbf{P}_{Nip}(1), \dots, ^I\mathbf{P}_{Nip}(64)\}$ (d) in 3D space. (b) Taking the positions of needle-tip of 64 frames of ultrasound-image manually. (e) The distributions of 64 true points, $\{^P\mathbf{P}_{Nip}(1), \dots, ^P\mathbf{P}_{Nip}(64)\}$, and its corresponding calibration points in 3D space. (an example of ICP algorithm)

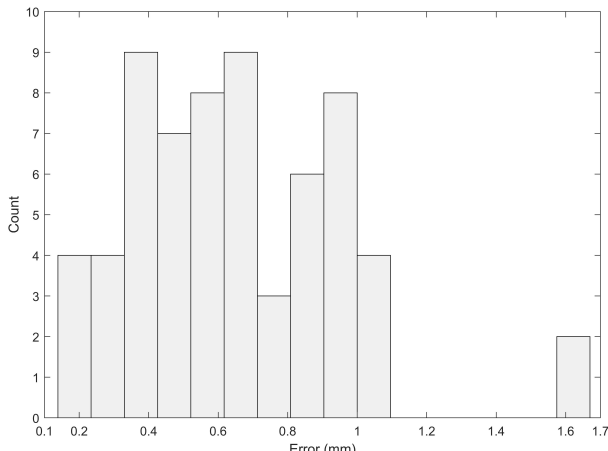


Fig. 11. The distribution histogram of 64 experimental errors (an example of ICP algorithm).

D. Comparison of the proposed method with Existing Methods

To thoroughly verify the effectiveness of the proposed method, we implemented an experimental comparison and a parametrical comparison of the proposed method with existing methods in this section, respectively.

1) *Experimental comparison:* In image-based calibration, the improved N-wire phantom method [22] and multi-wedge phantom method [25] are state-of-the-art. Therefore, we implemented the experimental comparison of these two methods with the proposed method for our previously developed US-guided dual-arm robotic brachytherapy system, respectively. The experimental setups of the improved N-wire

phantom method and the multi-wedge phantom method are shown in Fig. 12(a) and Fig. 12(b), respectively. A Polaris spectra optical tracker (Northern Digital Inc (NDI), Waterloo, Ontario, Canada) with two optical devices (each device contains four optical makers), an N-wire phantom, and a multi-wedge phantom are used here. The two optical devices are fixed on the phantom and robotic end-flange, respectively, and faced the NDI tracker. Then the transformation matrix between the two optical devices can be obtained by the NDI tracker directly. In this experiment, we first used the N-wire method and multi-wedge method to calibrate the transformation matrix $^{Pip}\mathbf{T}_I$, respectively. Then we took another 12 US images to test the calibration accuracy of the whole system (includes the needle, US probe, robotic arms, and the external optical tracker and phantom) based on the calibrated matrices $^{Pip}\mathbf{T}_I$ of the N-wire phantom method, multi-wedge phantom method, and the proposed method, respectively. The experimental results are shown in Table III.

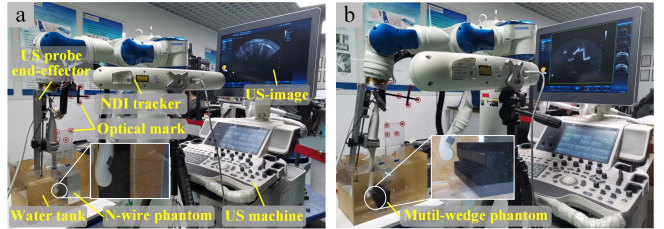


Fig. 12. Experimental setups of the N-wire phantom method (a) and the multi-wedge phantom method (b).

TABLE III.
EXPERIMENTAL COMPARISON OF THE PROPOSED METHOD
WITH IMAGE-BASED METHODS.

Method	Image-based Phantom	Calibration accuracy of the whole system		
		MAE (mm)	RMSE (mm)	SD (mm)
		N-wire [22]	3.51	4.18
		Multi-wedge [25]	3.11	3.19
Mechanism-image fusion-based registration algorithm (proposed method)	ICP	0.67	0.73	0.30
	Kabsch	0.72	0.77	0.29
	Landmark	0.72	0.77	0.29

As shown in Table III, our proposed mechanism-image fusion-based calibration method is significantly better than the other two image-based methods in terms of the calibration accuracy of the whole system. Specifically, considering the ICP algorithm as an example, the MAE, RMSE, and SD of the whole system in our proposed method are only 0.67 mm, 0.73 mm, and 0.30 mm, respectively. Those values are far less than the MAE (3.51 mm), RMSE (4.18 mm), and SD (2.26 mm) of the N-wire phantom calibration method and the MAE (3.11 mm), RMSE (3.19 mm), and SD (0.74 mm) of the multi-wedge phantom calibration method.

2) *Parametrical comparison:* In mechanism-based calibration, Shen *et al.* [27] proposed an arbitrary-wire phantom calibration method that is state-of-the-art. Therefore, we also implemented a parametrical comparison of the proposed method with this method. In this method, the calibration accuracy of the image of this method was

>>>>>>>>>>>>>>> File 1 Final version of the manuscript <<<<<<<<<<<<<<<<

8

1.022 ± 0.085 mm. In contrast, the calibration accuracy of the whole system of our proposed method is only 0.65 ± 0.31 mm. Therefore, the above results of both comparisons all justified the outperformance of the proposed method.

E. Evaluation of Execution Time

The whole procedure was implemented on a computer that has an Intel (R) Core (TM) i7-6700 CPU, 16GB RAM, and Windows 7 (64-bit) operating system. The total execution time includes two parts of mechanical calibration and US probe calibration, where most of the time is spent on taking sample data. Specifically, in the first part of the mechanical calibration, the execution time of taking sample data, including moving top-model-tip to reference-tip, moving needle-tip to reference-tip, moving probe-tip to reference-tip, moving the probe, and recording data, is about 5 minutes. But in practice operation, the time may be less or more than 5 minutes that is mainly affected by the operator familiarity. In the second part of the US probe calibration, the execution time of taking 64 sample data, including moving the probe 64 times, taking 64 US images, and marking the needle-tip position in these US images, is about 10 minutes. The number of taking sample data is directly related to execution time because it takes about 10 seconds to take a sample data. The attention here is that the positions of moving the probe 64 times can be designed by yourself before taking the experiment. This design will significantly help to reduce the time of taking sample data. For example, in our paper, 64 sample positions are designed to form a $40*40*40$ mm³ cube before experimenting. And in the process of marking the needle-tip position of the US image, all the needle-tip positions of these US images are automatically obtained by the program. On the other hand, the execution times of the data processing program of the two parts are all less than 1 second. Therefore, the entire calibration's execution time is about 15 minutes.

IV. DISCUSSION/

This paper proposed a mechanism-image fusion approach to the calibration of a US-guided dual-arm robotic brachytherapy system. The purpose of the experiments described in Section III was to determine how well the proposed approach could accomplish the accurate calibration of the US-guided dual-arm robotic brachytherapy system. These results showed that the calibration accuracy of the whole system was specifically high (0.65 ± 0.31 mm) and significantly better than that of the existing state-of-the-art methods. The primary reason is that one arm of the dual-arm robotic system is used as a substitute for tracker and phantom to calibrate the other arm. Therefore, with the proposed approach, no external tracker and complex phantom are needed, and then the errors of these external devices themselves cannot be accumulated. As a result, the proposed approach can ensure a sufficiently high calibration accuracy. Another possible reason is that the proposed approach is based on the high accuracy of the dual-arm robotic system. It ensures the reliability of the sample data.

On the other hand, existing calibration methods often need external tracker and phantom, which are not the control object of the needle insertion. Therefore, the calibration accuracy of

their methods could not be well maintained in the needle insertion process. For example, in [31], although it achieves a high accuracy of the US probe calibration in 1.04 mm, the accuracy during needle insertion was 2.28 mm and 3.86 mm at the apex and base of the prostate phantom, respectively. In contrast, by implementing the proposed calibration approach, the US probe calibration is based on the needle localization while the needle is also the controlled object of needle insertion. Therefore, the calibration accuracy of the system is improved while the needle insertion accuracy could be well maintained. This consistency is also a good advantage over existing methods.

However, the limitation of our approach is that the proposed calibration method is only suitable for dual/multiple-arm robotic systems and hard to be applied for single-arm robotic brachytherapy systems.

V. CONCLUSION AND FUTURE WORK

This paper presents a mechanism-image fusion approach to calibration of a US-guided dual-arm robotic brachytherapy system to ensure the high calibration accuracy of the whole system. With this approach, no external tracker or complex phantom is needed as the dual-arm robotic system can use one arm as a substitute for tracker and phantom to calibrate the other arm, which not results in accumulative errors. The needle-tip positions localized by the mechanism and image are utilized while the needle is also the controlled object of needle insertion. The experiments using three registration algorithms were performed, and then the calibration results were validated using the leave-one-out cross-validation method with our previously developed US-guided dual-arm robotic brachytherapy system. The results showed that the calibration accuracy of the whole system was effective using the proposed method. Besides, we also implemented the experimental comparison and parametrical comparison of the proposed method with the existing state-of-the-art methods. The results of both comparisons justified the outperformance of the proposed method. Furthermore, the whole calibration's execution time was evaluated at about 15 minutes.

In the future, to further improve the targeted accuracy of needle insertion, we will study how to reduce the error caused by the soft tissue deformation and how to adaptively control the interactional force between soft tissue and US probe. Furthermore, we will take the clinical trials of prostate brachytherapy. After that, we will apply this approach to our final US-guided dual-arm robotic brachytherapy system.

REFERENCES

- [1] American Cancer Society, "Cancer facts & figures 2020," Atlanta: American Cancer Society, 2020.
- [2] S. J. Henley *et al.*, "Annual Report to the Nation on the Status of Cancer, part II: Progress toward Healthy People 2020 objectives for 4 common cancers," *Cancer*, vol. 126, no. 10, pp. 2250-2266, Mar. 2020.
- [3] G. S. Fischer, I. C. Csoma, J. Tokuda, S. P. Dimaio, C. M. Tempany, N. Hata, and G. Fichtinger, "MRI-compatible pneumatic robot for transperineal prostate needle placement," *IEEE/ASME Trans. Mechatronics*, vol. 13, no. 3, pp. 295-305, Jun. 2008.
- [4] I. Hamdan, G. Dardenne, J. Bert, and D. Visvikis, "Non-rigid MRI/CT registration for effective planning of prostate brachytherapy," in *Proc.*

>>>>>>>>>>>>>>> File 1 Final version of the manuscript <<<<<<<<<<<<<<

9

- 38th Ann. Int. Conf. IEEE Engineering in Med. and Biol. Society. (EMBC)*, Orlando, FL, USA, 2016, pp. 1155-1158.
- [5] C. Tang, G. Xie, O. M. Omisore, J. Xiong, and Z. Xia, "A Real-time Needle Tracking Algorithm with First-frame Linear Structure Removing in 2D Ultrasound-guided Prostate Therapy," in *Proc. IEEE Int. Conf. Robotics and Biomimetics (ROBIO)*, Dali, China, 2019, pp. 1240-1245.
- [6] P. Stattin , E. Holmberg, J. E. Johansson, L. Holmberg, J. Adolfsson, and J. Hugosson, "Outcomes in localized prostate cancer: National prostate cancer registers of Sweden follow-up study," *J. National Cancer Institute*, vol. 102, no. 13, pp. 950-958, Jul. 2010.
- [7] C. Chira, G. Delouya, S. Larrive, J. F. Carrier, and D. Taussky, "Prostate volume changes during permanent seed brachytherapy: An analysis of intra-operative variations, predictive factors and clinical implication," *Radiation Oncology*, vol. 8, no. 1, pp. 177, 2013.
- [8] T. Podder, I. Buzurovic, K. Huang, and Y. Yu., "MIRAB: An image-guided multichannel robot for prostate Brachytherapy," *Int. J. Radiation Oncology Biol. Phys.*, vol. 78, no.3, pp. 209-213, Nov. 2010.
- [9] D. Stoianovici, C. Kim, F. Schafer, C. M. Huang, Y. Zuo, D. Petrisor, and M. Han, "Endocavity ultrasound probe manipulators," *IEEE/ASME Trans. Mechatronics*, vol. 18, no. 3, pp. 914-921, Jun. 2013.
- [10] H. Su, W. Shang, G. Cole, G. Li, K. Harrington, A. Camilo, J. Tokuda, C. M. Tempany, N. Hata, and G. S. Fischer, "Piezoelectrically actuated robotic system for MRI-guided prostate percutaneous therapy," *IEEE/ASME Trans. Mechatronics*, vol. 20, no. 4, pp. 1920-1932, Aug. 2015.
- [11] Y. Chen, A. Squires, R. Seifabadi, S. Xu, H. K. Agarwal, M. Bernardo, P. A. Pinto, P. Choyke, B. Wood, and Z. T. H. Tse, "Robotic system for MRI-guided focal laser ablation in the prostate," *IEEE/ASME Trans. Mechatronics*, vol. 22, no. 1, pp. 107-114, Feb. 2017.
- [12] N. Sarli, G. D. Giudice, S. De, M. S. Dietrich, S. D. Herrell, and N. Simaan, "TURBot: A system for robot-assisted transurethral bladder tumor resection," *IEEE/ASME Trans. Mechatronics*, vol. 24, no. 4, pp. 1452-1463, Aug. 2019.
- [13] G. R. Sutherland, S. Wolfsberger, S. Lama, and K. Zaeri-nia, "The evolution of neuroArm," *Neurosurgery*, vol. 72, no. 1, pp. A27-A32, Jan. 2013.
- [14] R. Kojcev, B. Fuerst, O. Zetting, J. Fotouhi, S. C. Lee, B. Frisch, R. Taylor, E. Sinibaldi, and N. Navalab, "Dual-robot ultrasound-guided needle placement: closing the planning-imaging-action loop," *Int. J. Computer Assist. Radio. Surg.*, vol. 11, no. 6, pp. 1173-1181, Jun. 2016.
- [15] J. Wang, L. Wu, M. Q. H. Meng, and H. Ren, "Towards simultaneous coordinate calibrations for cooperative multiple robots," in *Proc. IEEE International Conference on Intelligent Robots and Systems (IROS)*, Chicago, IL, USA, 2014, pp. 410-415.
- [16] Q. Ma, Z. Goh, and G. Chirikjian, "Probabilistic approaches to the AXB = YCZ calibration problem in multi-robot systems," *Auton. Robots*, vol. 42, pp. 1497-1520, Apr. 2018.
- [17] E. M. Boctor, A. Jain, M. A. Choti, R. H. Taylor, and G. Fichtinger, "Rapid calibration method for registration and 3D tracking of ultrasound images using spatial localizer," in *Proc. Conf. Medical Imaging 2003: Ultrasonic Imaging and Signal Processing (SPIE)*, 2003, pp. 521-532.
- [18] F. Vasconcelos, D. Peebles, S. Ourselin, and D. Stoyanov, "Spatial calibration of a 2D/3D ultrasound using a tracked needle," *Int. J. Computer Assist. Radio. Surg.*, vol. 11, no.6, pp. 1091-1099, Jun. 2016.
- [19] B. Lu, H. K. Chu, K. Huang, and J. Lai, "Surgical suture thread detection and 3-D reconstruction using a model-free approach in a calibrated stereo visual system," *IEEE/ASME Trans. Mechatronics*, vol. 25, no. 2, pp. 792-803, Apr. 2020.
- [20] L. Mercier , T. Lang , F. Lindseth, and L. D. Collins, "A review of calibration techniques for freehand 3-D ultrasound systems," *Ultrasound Med. Biol.*, vol. 31,no. 2, pp. 449-471, Apr. 2005.
- [21] T. K.Chen, A. D.Thurston, R. E. Ellis, P. Abolmaesumi, "A real-time freehand ultrasound calibration system with automatic accuracy feedback and control," *Ultrasound Med. Biol.*, vol. 35, no.1, pp. 79-93, Jan. 2009.
- [22] G. Carbalal, A. Lasso, A. Gómez, and G. Fichtinger, "Improving N-wire phantom-based freehand ultrasound calibration," *Int. J. Computer Assist. Radio. Surg.*, vol. 8, no. 6, pp. 1063-1072, Nov. 2013.
- [23] B. Mathieu, C. Claire, L. Lorenzo, and V. Arturo, "Temporal and spatial calibration of a freehand 3D ultrasound reconstructions system by using an N-wire phantom," in *Proc. 12th Int. Conf. Electrical Engineering, Computing Science and Automatic Control (CCE)*, Mexico City, Mexico, 2015, pp. 1-7.
- [24] H. K. Zhang, A. Cheng, Y. Kim, Q. Ma, G. S. Chirikjian, and E. M. Boctor, "Phantom with multiple active points for ultrasound calibration," *J. Med. Imaging*, vol. 5, no. 4, pp. 045001, Nov. 2018.
- [25] M. Najafi, N. Afsham, P. Abolmaesumi, and R. Rohling, "A closed-form differential formulation for ultrasound spatial calibration: multi-wedge phantom," *Ultrasound Med. Biol.*, vol. 40, no. 9, pp. 2231-2243, Sep. 2014.
- [26] F. Rousseau, P. Hellier, and C. Barillot, "Conflusius: A robust and fully automatic calibration method for 3D freehand ultrasound," *Med. Image Anal.*, vol. 9, no. 1, pp. 25-38, 2005.
- [27] C. Shen, L. Lyu, L. Wang, and J. Wu, "A method for ultrasound probe calibration based on arbitrary wire phantom," *Cogent Engineering*, vol. 6, no. 1, pp.1592739, Mar. 2019.
- [28] S. Alimohamadi, A. Ahmadian, and J. H. Bidgoli, "Ultrasound probe calibration using traceable frames of "V" phantom," in *Proc. 22nd Iranian Conf. Biomedical Engineering (ICBME)*, Tehran, Iran, 2015, pp. 319-324.
- [29] K. Li, J. Bai, Y. Chen, and X. Ji, "The calibration of targeting errors for an ultrasound-guided high-intensity focused ultrasound system," in *Proc. Conf. 2017 IEEE Int. Sym. on Med. Measurements and Applications (MeMeA)*, Rochester, MN, USA, 2017, pp. 10-14.
- [30] J. Shen, N. Zemiti, J. L. Dillenseger, and P. Poignet, "Fast and simple automatic 3D ultrasound probe calibration based on 3D printed phantom and an untracked marker," in *Proc. 40th Ann. Int. Conf. IEEE Engineering in Med. and Biol. Society (EMBC)*, Honolulu, HI, USA, 2018, pp. 878-882.
- [31] N. Hungr, M. Baumann, J. Long, and J. Troccaz, "A 3-D ultrasound robotic prostate brachytherapy system with prostate motion tracking," *IEEE Trans. Robotics*, vol. 28, no. 6, pp. 1382-1397, Dec. 2012.
- [32] C. Kim, D. Chang, D. Petrisor, G. Chirikjian, M. Han, and D. Stoianovici, "Ultrasound probe and needle-guide calibration for robotic ultrasound scanning and needle targeting," *IEEE Trans. Biomedical Engineering*, vol. 60, no. 6, pp. 1728-1734, Jun. 2013.
- [33] S. Lim, C. Jun, D. Chang, D. Petrisor, M. Han, and D. Stoianovici, "Robotic transrectal ultrasound guided prostate biopsy," *IEEE Trans. Biomedical Engineering*, vol. 66, no. 9, pp. 2527-2537, Sep. 2019.
- [34] YASKAWA, Slim dual-arm robot of Motoman SDA10F (2016). [Online]. Available: <https://www.motoman.com/industrial-robots/sda10f>
- [35] X. Wang and E. Red, "Robotic TCF and rigid-body calibration methods," *Robotica*, vol. 15, no. 6, pp. 633-644, Nov. 1997.
- [36] Y. Chen and G. Medioni, "Object modelling by registration of multiple range images," *Image Vision Comput.*, vol. 10, no. 3, pp. 145-155, 1992.
- [37] S. L. Davies, A. A. Neath, and J. E. Cavanaugh, "Cross validation model selection criteria for linear regression based on the Kullback-Leibler discrepancy," *Statistical Methodology*, vol. 2, no. 4, pp. 249-266, Dec. 2005.
- [38] P. Hsu, G. M. Treece, R. W. Prager, N. E Houghton, and A. H. Gee, "Comparison of freehand 3-D ultrasound calibration techniques using a stylus," *Ultrasound Med. Biol.*, vol. 34, no. 10, pp. 1610-1621, Oct. 2008.
- [39] F. S. Cheng. "Calibration of robot reference frames for enhanced robot positioning accuracy," *Robot Manipulators*, pp. 95-112, 2008.
- [40] W. Kabsch, "A solution for the best rotation to relate two sets of vectors," *Acta Crystallographica*, vol. 32, no. 5, pp. 922-923, Sep. 1976.
- [41] A. State, G. Hirota, D. T. Chen, W. F. Garrett, and M. A. Livingston, "Superior augmented reality registration by integrating landmark tracking and magnetic Tracking," in *Proc. 23rd ann. Conf. Comput. Graph. Interact. Tech.*, 1996, pp, 429-438.



Jing Xiong (M'13) received the B.S. degree and Ph.D. degree in mechanical engineering from Tsinghua University, China, in 2004 and 2010, respectively.

She is currently a full Professor at Shenzhen Institutes of Advanced Technology, Chinese Academy of Sciences, Shenzhen, China. She was or is the PI of over ten research grants including two National Natural Science Funds, and is the founder of two industrial joint labs. She has authored or coauthored over 60 peer-reviewed papers, and applied for over 70 patents. Her research interests include medical robotics, intelligent robotics, and image-guided therapy.

Dr. Xiong was recipient of the Wu Wenjun Artificial Intelligence Science and Technology Award (Natural Science)

>>>>>>>>>>>>>>> File 1 Final version of the manuscript <<<<<<<<<<<<<<<<

10

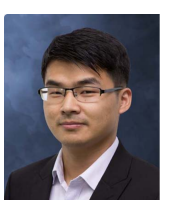
in 2017. She was the Program Co-Chair of IEEE RCAR 2019, and the Organizing Co-Chair of IEEE CYBER 2020.



Changfu Xu received the B.S. degree in Communication Engineering and M.S. degree in Software Engineering from Jiangxi University of Finance and Economics, China, in 2015 and 2018, respectively. He is currently a research assistant at Shenzhen Institutes of Advanced Technology, Chinese Academy of Sciences, Shenzhen, China. His research interests include surgical robotic systems and machine learning.



Khalil Ibrahim received the B.S. degrees in mechanical engineering from Assiut University, Egypt, in 2001, and the Ph.D. degree in Mechatronics and Robotics Engineering from Egypt-Japan University of Science and Technology, Egypt, in 2013. He is currently an assistant professor at Shenzhen Institutes of Advanced Technology, Chinese Academy of Sciences, Shenzhen, China. His research interests include surgical robot systems and minimally invasive surgery robot.



Hao Deng received the B.S. degree in mechanical engineering and automation from Wuhan University of Technology, Wuhan, China, in 2012, and the M.S. degree in mechatronic engineering from Harbin Institute of Technology, Shenzhen, China, in 2015. Since September 2017, he has been working toward the Ph.D. degree under the supervision of Prof. Zeyang Xia with Shenzhen Institutes of Advanced Technology, Chinese Academy of Sciences. His research interests include manipulation planning and control.



Zeyang Xia (SM'16) received the B.S. degree in mechanical engineering from Shanghai Jiao Tong University, Shanghai, China, in 2002, and the Ph.D. degree in mechanical engineering from Tsinghua University, Beijing, China, in 2008.

He is currently a full Professor at Shenzhen Institutes of Advanced Technology, Chinese Academy of Sciences, Shenzhen, China, where he is also the Director of Medical Robotics and Biomechanics Laboratory. He was or is the PI of over twenty research grants, including National Key Research and Development Project and four National Natural Science Funds. He has authored or coauthored over 100 peer reviewed papers, and applied for over 50 patents. His research interests include medical robotics, soft robotics, humanoid robotics, and biomechanics.

Dr. Xia was recipient of Guangdong Natural Science Funds for Distinguished Young Scholar in 2015, the Wu Wenjun Artificial Intelligence Science and Technology Award (Natural Science) in 2017, and Xiong Youlun Excellent Young Scholars Award in 2019, respectively. Dr. Xia is the Technical Editor of IEEE/ASME Transactions on Mechatronics. He was the General Chair of IEEE RCAR 2019 and key organizing

members of several other IEEE research conferences. He is the Chairman of Guangzhou Branch of the Youth Innovation Promotion Association, Chinese Academy of Sciences, and the Co-Chair of Guangdong Chapter of IEEE Robotics and Automation Society. Dr. Xia is a Fellow of IET starting 2019 and senior member of IEEE starting 2016.